

Physical Pictures for Quasisymmetry in Crystals

Bryan D. Assunção, Emmanuel V. C. Lopes, Tome M. Schmidt, and Gerson J. Ferreira
Instituto de Física, Universidade Federal de Uberlândia, Uberlândia, Minas Gerais 38400-902, Brazil

(Dated: February 23, 2026)

Quasisymmetry (QS) provides a novel route to understand and control near-degeneracies, Berry curvature, optical selection rules, and symmetry-protected phenomena in quantum materials. Here we give physical interpretations of the emergence of QS operators across multiple material families. Using density functional theory and the $\mathbf{k} \cdot \mathbf{p}$ formalism, we identify QS subspaces and calculate their representation matrices, quantifying the quasisymmetry via a metric ϵ that measures subspace invariance. For Sn/SiC and transition-metal dichalcogenide monolayers, QS corresponds to an emergent mirror symmetry, whereas in wurtzite crystals it manifests as an emergent spatial inversion. By contrast, for AgLa the QS appearing in avoided crossings is inherited from a nearby high-symmetry point rather than being an emergent lattice symmetry. Combining group-theoretical analysis and $\mathbf{k} \cdot \mathbf{p}$ modeling, our results establish concrete physical pictures for QS and provide practical criteria to diagnose it in first-principles calculations.

I. INTRODUCTION

Symmetry is fundamental to condensed matter physics, as it governs key properties such as electronic band structure, optical selection rules [1–6], and topological classification [7–11]. These principles have guided the discovery and engineering of advanced quantum materials, including topological (crystalline) insulators [12–21], Weyl and Dirac semimetals [22–26], topological superconductors [27–32], and altermagnets [33–36]. Since the early days, effective models are derived from symmetry principles via the theory of invariants [2], $\mathbf{k} \cdot \mathbf{p}$ [5] and tight-binding [37, 38] methods. Seminal works have used these approaches to describe essential materials, including Si and Ge [39], zincblende [40–43], and wurtzite [43–48] crystals. In the absence of inversion symmetry, symmetry constraints allow for Rashba and Dresselhaus spin-orbit couplings [49–51], which are crucial for spintronics [52]. Symmetry constraints are also essential to the development of novel materials for next-generation electronics, optoelectronics and energy storage, such as transition-metal dichalcogenides (TMDs) [53–68], Janus [69–72], perovskites [73–75], and MXenes [76–78] crystals.

Yet, many materials show near-degeneracies and selection rules beyond crystallographic symmetry constraints, pointing to approximate symmetries. In disordered topological materials, *ensemble averages* restore broken symmetries and produce topological Anderson insulators [79–82], for which the ensemble average of local invariants characterizes the topological phase [83–85]. In perovskites, ferroelectrics and multiferroics, *pseudosymmetries* occur when the crystal lattice is close to a higher-symmetry structure [86–89]. Particularly, in the *quasi-cubic* approximation [43–47], wurtzite crystals are approximated by a cubic zincblende structure strained along the (111) direction. Orbital-dependent site-permutation symmetries [90] can also extend beyond the crystal group and protect higher band degeneracies.

The recent proposal of *quasisymmetries* (QS) [91–93] provides a framework to understand approximate sym-

metries in quantum materials. In CoSi [91, 92], QS emerges as an angular momentum algebra protecting near-degeneracies and enhancing Berry curvature, which is detectable via quantum oscillations. Later, a classification of emergent QS groups, within the 32 point groups, has been developed in Ref. [93]. Quasisymmetry has since been identified in near-degenerate SOC gaps [94, 95], unconventional spin-polarizations [96], quantum spin Hall physics and topological quadrupoles [97–100], altermagnetism [101], asymmetrical Majorana bound states [102], Ising-type SOC in superconductors without M_z symmetry [103], and periodic dynamics in nonintegrable Hamiltonians [104, 105]. This variety of topics highlights the relevance of QS mechanisms to the design of advanced quantum materials, which motivates the question: what physical mechanisms drive the emergence of quasisymmetry in real materials?

In this paper, we identify two distinct physical pictures for quasisymmetries and verify them through first-principles calculations. In the first picture, the crystal group is augmented by an emergent symmetry arising from significant wavefunction localization on a sublattice. It occurs in Sn/SiC [94, 95] and TMD monolayers as mirror symmetries, and in wurtzite crystals as spatial inversion. Additionally, we argue that the quasi-cubic approximation for wurtzites is a special case of this first picture, where the approximation relies on compatibility relations rather than an emergent symmetry. In the second picture, quasisymmetry at generic \mathbf{k} -points arises from symmetry selection rules inherited from nearby high-symmetry points. It applies to AgLa [93], and possibly CoSi [91, 92] (see final remarks in the conclusions). We calculate the band structures and representation matrices for the QS operators, identifying quasi-irreps and quantifying quasisymmetry via a metric ϵ that measures subspace invariance. We focus on spin-orbit coupling (SOC) as the perturbation, though results can be extended to others, such as strain [93], electric fields and optical transitions. Using Löwdin’s perturbation theory [106], we compare the first and higher-order SOC gaps, verifying the QS suppression of the first order term.

This paper is organized as follows. Section II presents the theoretical framework including quasisymmetry formalism, the $\mathbf{k} \cdot \mathbf{p}$ picture, the metric ϵ , and the methodology to calculate the first-order SOC gap. Section III presents our results for various materials. Section IV summarizes conclusions. Throughout the paper, the DFT calculations were done with both Quantum Espresso [107, 108] and VASP [109, 110], Wannier models were obtained with wannier90 [111–113] and PythTB [114], representation matrices, symmetry analysis and effective models were developed via DFT2kp [115], IrRep [116], and Qsymm [117]. The computational details are presented in Appendices A and B.

II. QUASISYMMETRIES

Here we identify two distinct physical pictures for quasisymmetry. In Sec. II A, we show that sublattice localization can lead to emergent quasisymmetries that augment the crystal group following the hierarchy presented in Ref. [93]. In Sec. II B, we describe quasisymmetries inherited from nearby high-symmetry points using the $\mathbf{k} \cdot \mathbf{p}$ framework. Moreover, Sec. II C introduces the metric ϵ to quantify quasisymmetry, and Sec. II D presents perturbative SOC calculations.

A. Quasisymmetries I: emergent symmetry picture

We briefly review the framework introduced in Ref. [93], where quasisymmetry is described as additional symmetries acting within the first-order eigensubspace A of Löwdin's partitioning [106], leading to an augmented quasisymmetry group.

Generically, the Löwdin partitioning expresses the effective Hamiltonian H in terms of matrix elements of the unperturbed Hamiltonian H^0 and a perturbation H' as

$$H_{m,n} = E_n^0 \delta_{m,n} + H_{m,n}^{(1)} + H_{m,n}^{(2)} + \dots, \quad (1)$$

$$H_{m,n}^{(1)} = H'_{m,n}, \quad (2)$$

$$H_{m,n}^{(2)} = \frac{1}{2} \sum_{r \in B} H'_{m,r} H'_{r,n} \left(\frac{1}{E_m^0 - E_r^0} + \frac{1}{E_n^0 - E_r^0} \right), \quad (3)$$

where E_n^0 are the eigenenergies for each eigenstate $|n\rangle$ of H^0 , and $H'_{m,n} = \langle m | H' | n \rangle$ are the matrix elements of the perturbation. Here, $(m, n) \in A$ refer to the set A of eigenstates that constitute the subspace we want to model, while the summation in the second-order terms runs over the complementary set B of remote bands. The first-order term $H_{m,n}^{(1)}$ is entirely defined within A , while higher-order terms $H_{m,n}^{(n \geq 2)}$ require both sets $A \oplus B$.

Within the group-theoretical framework, the presence or absence of first-order couplings $H_{m,n}^{(1)}$ is dictated by the symmetry constraints. At a generic point \mathbf{k} , its little group $\mathcal{G}_{\mathbf{k}}$ is a subgroup of the crystal group \mathcal{G}_{Γ} . Labeling

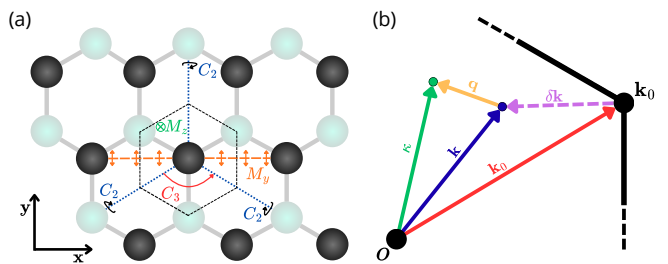


Figure 1. (a) Top view of a 2H transition metal dichalcogenide crystal lattice composed of two inequivalent sublattices: transition-metal sites (black), and chalcogen atoms (cyan). The full crystal group is D_{3h}^1 , which is generated by $C_3(z)$, $C_2(y)$ and M_z , while the isolated transition-metal sublattice is invariant under an additional symmetry M_y and transforms as the larger group $D_{6h}^1 = D_{3h}^1 \otimes \{E, M_y\}$. (b) Schematic representation of the \mathbf{k} -points used in the $\mathbf{k} \cdot \mathbf{p}$ expansion for the inheritance picture. The central point for the expansion is $\mathbf{k} = \mathbf{k}_0 + \delta\mathbf{k}$, which is near the high-symmetry point \mathbf{k}_0 . The Bloch theorem is initially written for a generic point $\boldsymbol{\kappa} = \mathbf{k} + \mathbf{q}$, and later we consider $\mathbf{q} = 0$.

the irreducible representations (irreps) of $\mathcal{G}_{\mathbf{k}}$ as $\Gamma_m^{(\mathbf{k})}$, the matrix element $H'_{m,n}$ can be finite if and only if $\Gamma_0^{(\mathbf{k})} \in \Gamma_m^{(\mathbf{k},*)} \otimes \Gamma_{H'}^{(\mathbf{k})} \otimes \Gamma_n^{(\mathbf{k})}$, where $\Gamma_0^{(\mathbf{k})}$ is the trivial irrep.

As shown in Ref. [93], the basis functions for certain subspaces A of $\mathcal{G}_{\mathbf{k}}$ are invariant under emergent quasisymmetries $Q = \{Q_1, Q_2, \dots\}$. They obey selection rules for an augmented quasisymmetry group $\mathcal{G}_Q = \mathcal{G}_{\mathbf{k}} \otimes Q$ for which $\Gamma_0^{(Q)} \notin \Gamma_m^{(Q,*)} \otimes \Gamma_{H'}^{(Q)} \otimes \Gamma_n^{(Q)}$. The quasisymmetry then imposes vanishing first-order terms $H_{m,n}^{(1)} = H'_{m,n} \equiv 0$, making the second-order term $H_{m,n}^{(2)}$ in Eq. (1) the leading-order perturbation for $H_{m,n}$, where $H'_{m,r}$ obeys selection rules strictly from $\mathcal{G}_{\mathbf{k}}$ since $r \in B$.

This framework is insightful, but it does not provide an interpretation of why and when such quasisymmetries emerge. Here, we identify that the extra symmetries arise due to significant wave function localization on a single sublattice, which is invariant under an additional symmetry Q that does not belong to the crystal group, as shown in Fig. 1(a). The quasisymmetry Q must be consistent with the little group $\mathcal{G}_{\mathbf{k}}$ of the \mathbf{k} -point of interest to consistently generate the augmented group $\mathcal{G}_Q = \mathcal{G}_{\mathbf{k}} \otimes Q$.

In Section III, we show that for Sn/SiC [94, 95] and TMDs the quasisymmetry is a mirror, while for wurtzites it is spatial inversion. Additionally, in Sec. III A 3 we show that the quasi-cubic approximation for wurtzites is a special case of this first picture, where the augmented group \mathcal{G}_Q is built from compatibility relations rather than a direct product with an emergent symmetry Q .

B. Quasisymmetries II: inheritance picture

The second quasisymmetry picture is due to the residual influence of a nearby high-symmetry point \mathbf{k}_0 . Eigenstates at $\mathbf{k} = \mathbf{k}_0 + \delta\mathbf{k}$ approximately obey selection rules

inherited from the nearby \mathbf{k}_0 point, little group $\mathcal{G}_{\mathbf{k}_0} > \mathcal{G}_{\mathbf{k}}$, when sufficiently isolated from remote bands.

To formulate this picture, we express the $\mathbf{k} \cdot \mathbf{p}$ framework with the Bloch theorem written as

$$\psi_{n,\boldsymbol{\kappa}}(\mathbf{r}) = e^{i\boldsymbol{\kappa} \cdot \mathbf{r}} u_{n,\boldsymbol{\kappa}}(\mathbf{r}) = e^{i\mathbf{q} \cdot \mathbf{r}} \phi_{n,\boldsymbol{\kappa},\mathbf{q}}(\mathbf{r}), \quad (4)$$

$$\phi_{n,\boldsymbol{\kappa},\mathbf{q}}(\mathbf{r}) = e^{i(\boldsymbol{\kappa}-\mathbf{q}) \cdot \mathbf{r}} u_{n,\boldsymbol{\kappa}}(\mathbf{r}), \quad (5)$$

where $u_{n,\boldsymbol{\kappa}}(\mathbf{r})$ is the periodic part of the Bloch function $\psi_{n,\boldsymbol{\kappa}}(\mathbf{r})$. Figure 1(b) illustrates the k-points: $\boldsymbol{\kappa} = \mathbf{k} + \mathbf{q}$ is generic, \mathbf{k}_0 is a high-symmetry point, $\mathbf{k} = \mathbf{k}_0 + \delta\mathbf{k}$ is the central point of interest, and \mathbf{q} is the deviation from \mathbf{k} . The $\mathbf{k} \cdot \mathbf{p}$ Hamiltonian acting on $\phi_{n,\boldsymbol{\kappa},\mathbf{q}}(\mathbf{r})$ is $H = H^0 + H^{\text{SOC}} + 2\mathbf{q} \cdot \boldsymbol{\pi}$, with

$$H^0 = p^2 + V(\mathbf{r}) + q^2, \quad (6)$$

$$H^{\text{SOC}} = \mathbf{H}_\sigma \cdot \boldsymbol{\sigma}, \quad (7)$$

$$\mathbf{H}_\sigma = \frac{\alpha^2}{4} (\nabla V \times \mathbf{p}). \quad (8)$$

The orbital part $\mathbf{H}_\sigma = (H_x, H_y, H_z)$ of the spin-orbit coupling is defined to be used later, $V(\mathbf{r})$ is the crystalline potential, $\boldsymbol{\pi} = \mathbf{p} + \alpha^2 \boldsymbol{\sigma} \times \nabla V / 8$ is the generalized momentum with SOC contributions, and $\alpha \approx 1/137$ is the fine structure constant. We use atomic Rydberg

units, with $\hbar = 2m_0 = 1$. Hereafter, we focus on the central point of the $\mathbf{k} \cdot \mathbf{p}$ expansion $\boldsymbol{\kappa} \equiv \mathbf{k}$, with $\mathbf{q} = 0$.

Consider that two eigenstates $|m, \mathbf{k}\rangle$ and $|n, \mathbf{k}\rangle$ of H^0 cross at \mathbf{k} with energies $E_m(\mathbf{k}) = E_n(\mathbf{k})$. Including SOC perturbatively, i.e., $H' = H^{\text{SOC}}$, the first-order coupling to induce an anticrossing would be $\langle m, \mathbf{k} | H' | n, \mathbf{k} \rangle$. To apply selection rules to this matrix element, we must consider the irreps of its constituents on the little group $\mathcal{G}_{\mathbf{k}}$, such that the matrix element is finite if and only if $\Gamma_m^{(\mathbf{k},*)} \otimes \Gamma_{H'}^{(\mathbf{k})} \otimes \Gamma_n^{(\mathbf{k})} \supseteq \Gamma_0^{(\mathbf{k})}$.

If $\mathbf{k} \approx \mathbf{k}_0$, we can approximate

$$u_{n,\mathbf{k}}(\mathbf{r}) \simeq u_{n,\mathbf{k}_0}(\mathbf{r}) + \sum_{m \neq n} \frac{\delta\mathbf{k} \cdot \mathbf{p}_{m,n}}{\Delta_{n,m}} u_{m,\mathbf{k}_0}(\mathbf{r}), \quad (9)$$

where both the energy difference $\Delta_{nm} = E_n(\mathbf{k}_0) - E_m(\mathbf{k}_0)$ and $\mathbf{p}_{m,n} = \langle m, \mathbf{k}_0 | \mathbf{p} | n, \mathbf{k}_0 \rangle$ are evaluated at \mathbf{k}_0 . The second term can be neglected when $\mathbf{p}_{m,n}$ vanishes by symmetry or when Δ_{nm} is large, $|\delta\mathbf{k} \cdot \mathbf{p}_{m,n} / \Delta_{n,m}| \ll 1$, yielding $u_{n,\mathbf{k}}(\mathbf{r}) \approx u_{n,\mathbf{k}_0}(\mathbf{r})$. Equation (5) then becomes

$$\phi_{n,\mathbf{k}}(\mathbf{r}) \equiv e^{i\mathbf{k} \cdot \mathbf{r}} u_{n,\mathbf{k}}(\mathbf{r}) \approx e^{i\delta\mathbf{k} \cdot \mathbf{r}} \phi_{n,\mathbf{k}_0}(\mathbf{r}), \quad (10)$$

where we now omit the $\mathbf{q} = 0$ index for simplicity. Notice that $\phi_{n,\mathbf{k}_0}(\mathbf{r}) = e^{i\mathbf{k}_0 \cdot \mathbf{r}} u_{n,\mathbf{k}_0}(\mathbf{r})$ is an eigenstate of H^0 at the high-symmetry point \mathbf{k}_0 .

The approximation above allows us to write the matrix element of H^{SOC} as

$$\langle m, \mathbf{k} | H' | n, \mathbf{k} \rangle = \langle m, \mathbf{k}_0 | e^{-i\delta\mathbf{k} \cdot \mathbf{r}} H' e^{i\delta\mathbf{k} \cdot \mathbf{r}} | n, \mathbf{k}_0 \rangle = \frac{\alpha^2}{4} \langle m, \mathbf{k}_0 | [\nabla V \times (\mathbf{p} + \delta\mathbf{k})] \cdot \boldsymbol{\sigma} | n, \mathbf{k}_0 \rangle, \quad (11)$$

which can now be evaluated under the selection rules of $\mathcal{G}_{\mathbf{k}_0}$ for the high-symmetry point \mathbf{k}_0 instead of $\mathcal{G}_{\mathbf{k}} < \mathcal{G}_{\mathbf{k}_0}$.

In AgLa [93] (Sec. IIIB), selection rules from $\mathcal{G}_{\mathbf{k}}$ allow for a finite $\langle m, \mathbf{k} | H' | n, \mathbf{k} \rangle$, but stronger constraints from $\mathcal{G}_{\mathbf{k}_0}$ show that only the $\delta\mathbf{k}$ -term in Eq. (11) contributes, while the \mathbf{p} -term vanishes by symmetry. However, the $\delta\mathbf{k}$ -term contribution to SOC is typically small and can be neglected. Thus, Eq. (11) reduces to $\langle m, \mathbf{k} | H' | n, \mathbf{k} \rangle = \langle m, \mathbf{k}_0 | H' | n, \mathbf{k}_0 \rangle$. The left-hand side obeys selection rules from $\mathcal{G}_{\mathbf{k}}$, while the right-hand side obeys constraints from $\mathcal{G}_{\mathbf{k}_0}$. Therefore, all symmetries in $\mathcal{G}_{\mathbf{k}_0}$ that are not in $\mathcal{G}_{\mathbf{k}}$ act as inherited quasisymmetries at \mathbf{k} .

C. Quasisymmetry metric ϵ and quasi-irreps

We quantify quasisymmetry by measuring how closely a subset A is invariant under a proposed QS operator Q . If A is invariant under Q , the action of Q is closed within A . In a block representation of Q in the basis $A \oplus B$,

$$Q = \begin{pmatrix} Q_{AA} & Q_{AB} \\ Q_{BA} & Q_{BB} \end{pmatrix}, \quad (12)$$

closure of A under Q requires $Q_{AB} = 0$. Since Q is unitary, this implies Q_{AA} is unitary. Conversely, if Q_{AA}

is unitary, then A is invariant under Q . Therefore, we quantify quasisymmetry by measuring how close Q_{AA} is to unitary with the metric

$$\epsilon = \sqrt{\frac{1}{N_A} \text{Tr}[P_A Q^\dagger P_A Q]}, \quad (13)$$

where $P_A = \sum_{n \in A} |n\rangle\langle n|$ is the projection operator into subspace A , and N_A is its dimension. The metric $\epsilon \in [0, 1]$ reaches $\epsilon \equiv 1$ if and only if A is exactly invariant under Q . When $\epsilon \approx 1$, Q is a quasisymmetry, and this matrix representation identifies quasi-irreps $\Gamma_n^{(Q)}$ of \mathcal{G}_Q constituting the subspace A .

D. SOC as perturbation

Quasisymmetry implies that within the QS subspace, the first-order matrix element $\langle m | H^{\text{SOC}} | n \rangle \approx 0$. Since quasisymmetry is not exact, this element does not vanish identically. We develop a numerical approach to calculate this matrix element using DFT and wannierization via

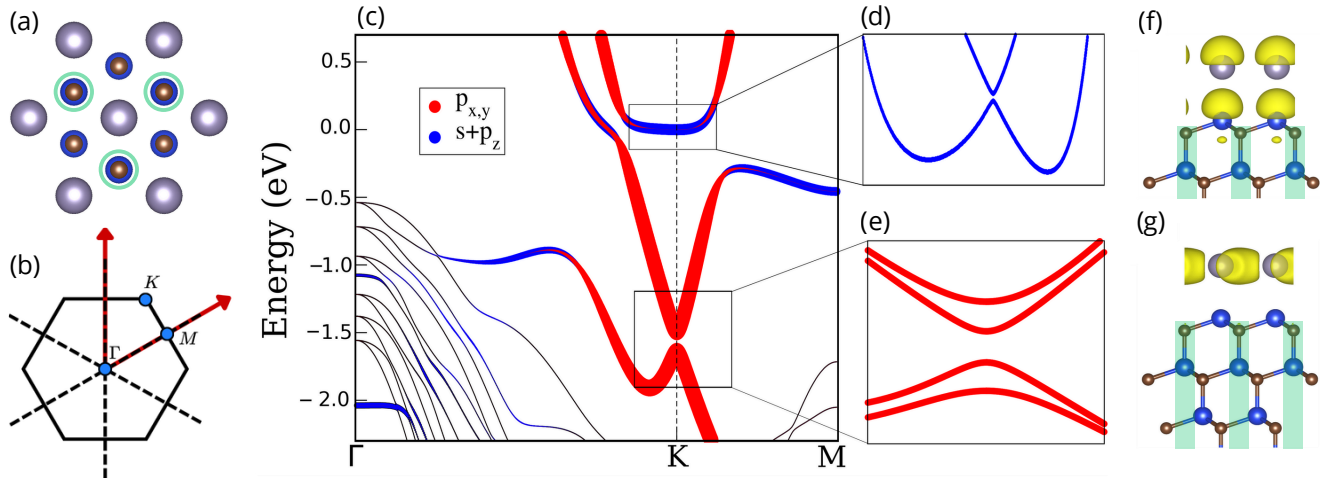


Figure 2. (a) Crystal structure of the Sn/SiC(0001)-1 \times 1 surface, where Sn atoms are adsorbed on top of surface Si atoms (on-top sites). Gray, blue, and brown spheres denote Sn, Si, and C atoms, respectively. The green contours highlight one of the two distinct Si-C stacking sequences not aligned with Sn atoms, as also illustrated in panels (f) and (g). (b) Corresponding Brillouin zone with high-symmetry points indicated. (c) Spin-orbit-free band structure projected onto Sn $s + p_z$ (blue) and $p_x + p_y$ (red) orbitals. Contributions from Si and C atoms are negligible in the energy window of interest and are therefore not shown. (d) Rashba-like (RL) spin splitting near the K point, with a SOC-induced gap of approximately 2 meV. (e) Zeeman-like (ZL) spin splitting near K, with a SOC-induced gap of approximately 157 meV. (f,g) Charge density distribution associated with the RL and ZL bands, respectively.

wannier90. The $\mathbf{k} \cdot \mathbf{p}$ method cannot be used for this purpose due to DFT limitations (see Appendix B).

We generate *ab initio* band structures with both scalar relativistic (SR, without SOC) and fully relativistic (FR, with SOC) pseudopotentials using QE. From these, we build tight-binding models H_{SR} and H_{FR} . To compare H_{SR} and H_{FR} , both models must be written in compatible basis sets. This is nontrivial, since maximal localization in wannier90 can yield different Wannier functions for H_{SR} and H_{FR} . To ensure consistency, we use the same initial projections for both H_{SR} and H_{FR} , and use one of the following approaches: skip maximal localization (`num_iter` = 0), use symmetry-adapted Wannier functions [118, 119], or the selectively localized Wannier functions method [120].

Assuming the basis sets are consistent, we define

$$H^{\text{SOC}} \approx H_{FR} - H_{SR} \otimes \sigma_0, \quad (14)$$

where σ_0 is the identity in spin space. The atomic form $H^{\text{SOC}} \approx \sum_i \lambda_i \mathbf{L}_i \cdot \mathbf{S}$ is obtained only when Wannier functions resemble atomic orbitals, which is not guaranteed in general. Nevertheless, even when this is not the case, projecting H^{SOC} into the eigenstates of $H_{SR} \otimes \sigma_0$ at the k-point of interest allows us to directly compare with $\mathbf{k} \cdot \mathbf{p}$ models and identify matrix element values.

III. RESULTS

We illustrate examples of both the emergent-symmetry and inheritance pictures for quasisymmetry. For the

emergent-symmetry picture we consider Sn/SiC, monolayer TMDs, and wurtzite materials. The metric ϵ is calculated for examples from the emergent-symmetry picture: Sn/SiC, TMDs and wurtzites. The intensity of first-order SOC is calculated for the TMDs only, since for Sn/SiC we could not guarantee the basis set consistency between H_{SR} and H_{FR} due to highly entangled bands, and for wurtzites the relevant perturbation is the crystal field, not SOC. For the inheritance picture we consider AgLa, where we identify that the first-order SOC is dominated by the $\delta\mathbf{k}$ -term in Eq. (11). Throughout the paper, the single group irrep nomenclature follows Mulliken Symbols [121], while the double group irrep classification is based on Koster's book [1] and the Bilbao Crystallographic Server [122–124].

A. Quasisymmetries I: emergent symmetry picture

1. Sn/SiC

We consider the Sn/SiC(0001)-1 \times 1 surface, a triangular lattice of Sn atoms adsorbed on a 6H-SiC (0001) substrate [Fig. 2(a)]. The Brillouin zone is shown in Fig. 2(b). This system hosts quasi-degenerate states near the K point, with conflicting interpretations in the literature [94, 95]. In Ref. [94], the authors explain the near degeneracy as an emergent mirror M_y due to the wavefunction localization along atoms aligned with the Sn sublattice. Interestingly, their explanation was developed prior to the quasisymmetry proposal [91], and

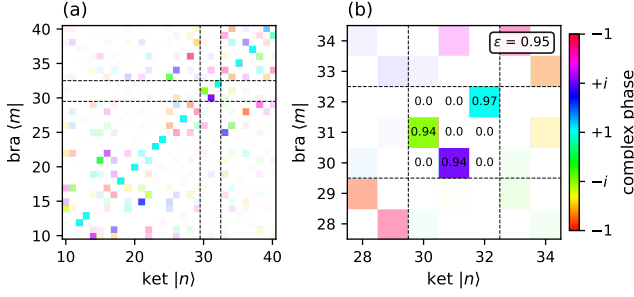


Figure 3. Complex matrix $Q_{m,n} = \langle m|M_y|n\rangle$, with the RL and ZL subspaces highlighted by the dashed lines. The values within the squares of the diagram correspond to $|Q_{m,n}|^2$, which also defines the color intensity, while the color itself represents the complex phase of the matrix element. The matrix is shown on a large scale in (a), while in (b) we zoom into the RL and ZL subspaces.

it matches our emergent symmetry picture. In contrast, Ref. [95] assumes atomistic SOC to identify an $SU(2)$ quasisymmetry. We unify this apparent discrepancy by showing that the mirror M_y quasisymmetry is consistent with the $SU(2)$ interpretation of Ref. [95], where M_y and its C_3 -conjugated partners act as spin rotations within the quasisymmetric subspace.

The band structure without SOC [Fig. 2(c)] shows spin-degenerate bands near the Fermi level. With SOC, a small gap of ~ 2 meV emerges at K [Fig. 2(d)], forming a Rashba-like (RL) splitting. Neighboring bands exhibit

Zeeman-like (ZL) behavior with a much larger SOC gap [Fig. 2(e)]. These contrasting scales suggest quasisymmetries. The RL bands (dominated by s and p_z orbitals from Sn atoms and underlying SiC) are localized beneath the Sn sublattice. Although the little group C_3 at K lacks mirror symmetry, this orbital localization [Figs. 2(f-g)] suggests emergent mirror symmetry M_y [94] within both RL and ZL subspaces.

To quantify quasisymmetry beyond visual orbital arguments, Fig. 3 shows the matrix elements $Q_{m,n} = \langle m|M_y|n\rangle$. The Q matrix within both RL and ZL subspaces is nearly unitary, yielding $\epsilon = 0.968$ for the combined subspace. This confirms that M_y reflects a robust constraint on the wavefunctions.

The M_y quasisymmetry extends the group to $C_{3v} = C_3 \otimes \{E, M_y\}$ within both the RL and ZL regions. The RL pair $\{|R, \uparrow\rangle, |R, \downarrow\rangle\}$ forms a two-dimensional subspace, whose orbital part transforms as the irrep A of C_3 , which becomes the quasi-irrep A_1 under C_{3v} . Under the crystal group C_3 the selection rules for the z-component of the orbital part of the SOC matrix element, $\langle R|H_z|R\rangle$ [see Eq. (8)], give us $A \otimes A \otimes A = A$, indicating it is finite. However, under the QS group C_{3v} the first-order matrix element vanishes, since now we have $A_1 \otimes A_2 \otimes A_1 = A_2$. The ZL set $\{|Z_+, \uparrow\rangle, |Z_+, \downarrow\rangle, |Z_-, \uparrow\rangle, |Z_-, \downarrow\rangle\}$ also transforms under the QS group C_{3v} , but it does not enjoy this cancellation, since under C_3 the selection rules read $E \otimes A \otimes E = 2A \oplus E$, and for the QS group it reads $E \otimes A_2 \otimes E = A_1 \oplus A_2 \oplus E$, such that both cases include the trivial irrep or quasi-irrep. More generally, the effective Hamiltonian at K under the basis composed of the RL and ZL bands reads as

$$H(K) = \begin{pmatrix} \epsilon_0^R + \delta_z^{R,R} & 0 & 0 & 0 & 0 & \Delta_x^{R,Z-} \\ 0 & \epsilon_0^R - \delta_z^{R,R} & -\Delta_x^{R,Z+} & 0 & 0 & 0 \\ 0 & -\Delta_x^{R,Z+} & \epsilon_0^{Z+} + \Delta_z^{Z+} & 0 & 0 & 0 \\ 0 & 0 & 0 & \epsilon_0^{Z+} - \Delta_z^{Z+} & -i\Delta_y^{Z+,Z-} & 0 \\ 0 & 0 & 0 & i\Delta_y^{Z+,Z-} & \epsilon_0^{Z-} - \Delta_z^{Z-} & 0 \\ \Delta_x^{R,Z-} & 0 & 0 & 0 & 0 & \epsilon_0^{Z-} + \Delta_z^{Z-} \end{pmatrix}, \quad (15)$$

where ϵ_0^n is the contribution from H^0 , $\Delta_i^{n,m}$ and $\delta_i^{n,m}$ are the σ_i SOC terms. The $\Delta_i^{n,m}$ terms are allowed in both the crystal group C_3 and the QS group C_{3v} , while the $\delta_i^{n,m}$ vanish in the QS group. The Hamiltonian above was obtained by imposing the symmetry constraints of the crystal and QS groups via the theory of invariants [2] with the Qsymm code [117]. The vanishing of the $\delta_i^{n,m}$ terms indicates that the small SOC gap in RL bands arises, to leading order, from second-order contributions from $\Delta_x^{R,Z+} \approx \Delta_x^{R,Z-}$, which are constrained to be equal by the quasisymmetry, as well as the intraband couplings $\Delta_z^{Z+} \approx \Delta_z^{Z-}$ within the ZL sector.

To connect the M_y quasisymmetry with the $SU(2)$ symmetry proposed in Ref. [95], notice that within the RL subspace the orbitals transform as the trivial A_1 quasi-irrep of C_{3v} single group. Introducing the spin, the double group quasi-irrep becomes $A_1 \otimes D_{1/2} = D_{1/2}$, where $D_{1/2}$ is the spin 1/2 representation. Therefore, within this quasi-irrep the $M_y \in SU(2)$ and its conjugated partners in C_{3v} , constitute a sufficient subset of $SU(2)$ operators that defines quasisymmetry in Sn/SiC.

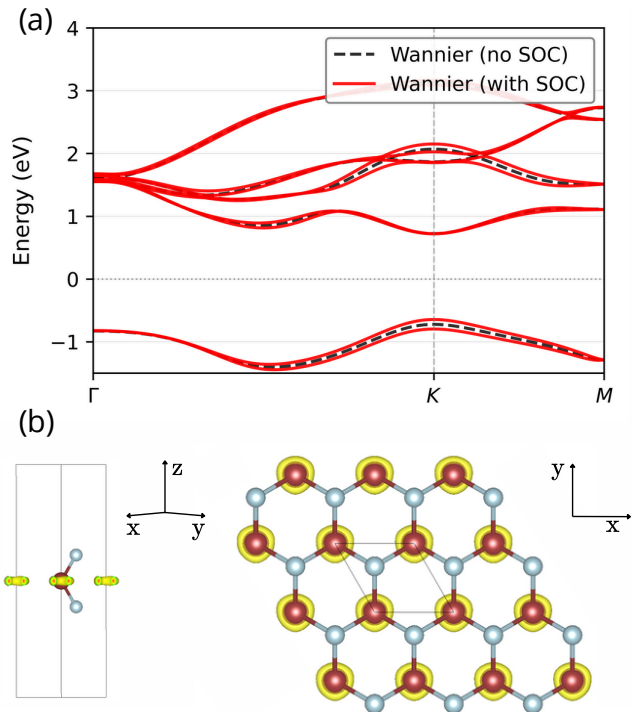


Figure 4. (a) Band structure of MoS₂ calculated using Quantum ESPRESSO and Wannier90, without SOC (black dashed lines) and with SOC (red solid lines). (b) Side and top views of the charge density associated with the first conduction band of MoS₂ at K. The brown and cyan spheres represent Mo and S atoms, respectively, while the yellow isosurfaces correspond to the real-space charge density $|\psi(\mathbf{r})|^2$.

2. Monolayer TMDs

A similar mechanism appears in monolayer TMDs such as MoS₂ and WSe₂, which belong to space group $P\bar{6}m2$ (D_{3h}^1) and exhibit unusually small SOC splitting in the first conduction band at the K point (little group C_{3h}), as shown in Fig. 4. The standard explanation from Ref. [125] uses a tight-binding model with $H_{\text{SOC}} = \lambda \mathbf{L} \cdot \mathbf{S}$, justified by strong Wannier orbital localization. The $m = 0$ character of the dominant d_{z^2} orbital suppresses first-order SOC. This interpretation is correct within the spherical $\mathbf{L} \cdot \mathbf{S}$ approximation.

Our quasisymmetry analysis generalizes this result. As shown in Fig. 4(b), the conduction-band wavefunction is strongly localized on the transition-metal sublattice, yielding an M_y mirror quasisymmetry, enlarging the low-energy subspace symmetry to $D_{3h} = C_{3h} \otimes \{E, M_y\}$. The M_y matrices in Figs. 5(a-d) confirm approximate unitary structure with $\epsilon > 0.95$ for both MoS₂ and WSe₂. Consequently, as in Sn/SiC, matrix elements of H_{SOC} are suppressed by the full operator $\nabla \mathbf{V} \times \mathbf{p}$, not only by its atomic-limit \mathbf{L} .

To quantify the first and higher order contributions to the SOC gap, we construct a Wannier representation us-

ing Wannier90. The Wannier band structure [Fig. 4(a)] matches established DFT data for MoS₂ [125, 126]. The effective model at K reads $H_K = \lambda_V \sigma_z$, where λ_C and λ_V are SOC intensities in conduction and valence bands. Following Sec. IID, we find that the first-order contribution, $\lambda_C^{(1)} \approx 1.78$ meV, consists of $\sim 60\%$ of the total SOC gap $\lambda_C \approx 3.04$ meV in the conduction band, i.e., the first order contribution is comparable to the second and higher order corrections, confirming that quasisymmetry suppresses the first-order term. In the valence band, which is not quasisymmetric, $\lambda_V^{(1)} \approx 153.7$ meV nearly equals the full gap $\lambda_V \approx 153.8$ meV. Similar behavior appears in WSe₂: for the conduction band the first order contribution is $\lambda_C^{(1)} = 10.6$ meV, corresponding to $\sim 25\%$ out of the total $\lambda_C = 40.6$ meV, while for the valence band $\lambda_V^{(1)} = 488$ meV, and $\lambda_V = 475$ meV.

3. Wurtzites

Wurtzite materials such as GaN, GaP, and ZnO belong to space group $P6_3mc$ (C_{6v}^4) with little group C_{6v} at Γ . Their band structures are commonly modeled using the quasi-cubic approximation [43–47], treating wurtzite as a strained zincblende (space group $F\bar{4}3m$ or T_d^2) along the [111] direction. Thus, the quasi-cubic approximation can be interpreted as a *pseudosymmetry*, assuming the wurtzite lattice is close to a cubic one. This can now be interpreted as a special case from the first quasisymmetry picture. Since C_{6v}^4 is not a subgroup of T_d^2 , the quasi-cubic approximation does not involve direct group extension as in picture I. Instead, it operates through compatibility relations established via the common subgroup $C_3^1 \subset C_{6v}^4$ and $C_3^1 \subset T_d^2$. Additionally, we introduce a second quasisymmetry for wurtzites based on spatial inversion \mathcal{I} , yielding the QS group $D_{6h}^4 = C_{6v}^4 \otimes \{E, \mathcal{I}\}$, and compare its constraints with those from the quasi-cubic approximation. The compatible irreps for each band under the C_{6v}^4 , T_d^2 and D_{6h}^4 groups are shown in Table I.

A typical band structure for wurtzite crystals is shown in Fig. 6(a) for GaN. The top valence bands are composed by p-like orbitals split into the C_{6v}^4 irreps Γ_5 for $|X \pm iY\rangle$, and Γ_1 for $|Z\rangle$ due to the hexagonal crystal field. The $6 \times 6 \mathbf{k} \cdot \mathbf{p}$ Hamiltonian including SOC [5, 46] reads

$$H_{\text{WZ}} = \begin{pmatrix} F & -K^* & -H^* & 0 & 0 & 0 \\ -K & G & H & 0 & 0 & \Delta \\ -H & H^* & \lambda & 0 & \Delta & 0 \\ 0 & 0 & 0 & F & -K & H \\ 0 & 0 & \Delta & -K^* & G & -H^* \\ 0 & \Delta & 0 & H^* & -H & \lambda \end{pmatrix}, \quad (16)$$

where $F = E_v + \Delta_1 + \Delta_2 + \lambda + \theta$, $G = E_v + \Delta_1 - \Delta_2 + \lambda + \theta$, $\lambda = E_v + A_1 k_z^2 + A_2(k_x^2 + k_y^2)$, $\theta = A_3 k_z^2 + A_4(k_x^2 + k_y^2)$, $K = A_5 k_+^2$, $H = A_6 k_+ k_z + i A_7 k_+$, $\Delta = \sqrt{2} \Delta_3$, and $k_{\pm} = k_x \pm i k_y$. The parameters Δ_i represent crystal-field

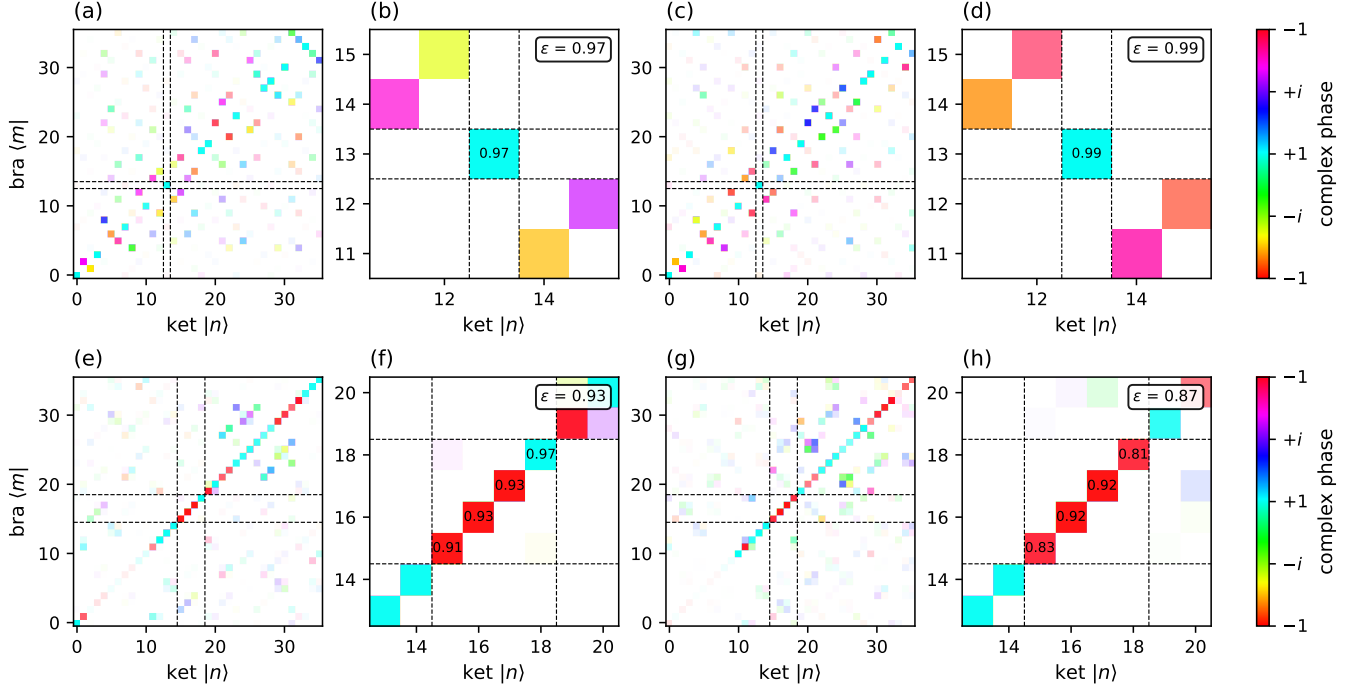


Figure 5. (a,c) Complex matrices $Q_{m,n} = \langle m | \mathcal{M}_y | n \rangle$ for the TMD monolayers MoS₂ and WSe₂, respectively. The regions enclosed by dashed lines correspond to the QS subspaces. (b,d) Zoom into the QS subspaces of (a,c). (e,g) Equivalent matrices, $Q_{m,n} = \langle m | \mathcal{I} | n \rangle$, for the wurtzites GaN and GaP, respectively, and zoom into the QS subspaces shown in (f,h). The color codes and labels are equivalent to those in Fig. 3.

Table I. Irreps of the valence and conduction bands of wurtzite materials under the crystal group C_{6v}^4 , the inversion quasisymmetry group D_{6h}^4 , and the quasi-cubic quasisymmetry group T_d^2 . For the T_d^2 group the $[X(X^2 - 3Y^2)]$ -like orbital is part of a three-dimensional irrep and its compatibility with its C_{6v}^4 and D_{6h}^4 counterparts is ill-defined. For each group the top lines refer to the single group irreps, while the bottom lines refer to the corresponding double group irreps [1, 122–124].

	Valence (X, Y, Z)	Conduction GaN S	Conduction GaP $X(X^2 - 3Y^2)$
C_{6v}^4	$\Gamma_1 \oplus \Gamma_5$ $2\Gamma_7 \oplus \Gamma_9$	Γ_1 Γ_7	Γ_3 Γ_8
D_{6h}^4	$\Gamma_2^- \oplus \Gamma_6^-$ $2\Gamma_7^- \oplus \Gamma_9^-$	Γ_1^+ Γ_7^+	B_{1u} Γ_8^-
T_d^2	Γ_4 $\Gamma_7 \oplus \Gamma_8$	Γ_1 Γ_6	- -

and SOC splittings, while A_i are effective mass parameters. This model includes all symmetry-allowed couplings within the C_{6v}^4 group, neglecting only the k-dependent SOC (kSOC). For the full model, including kSOC, see [127, 128]. Particularly, the valence band energies and

SOC terms are defined by the matrix elements

$$E_v = \langle Z | H^0 | Z \rangle, \quad (17)$$

$$E_v + \Delta_1 = \langle X | H^0 | X \rangle = \langle Y | H^0 | Y \rangle, \quad (18)$$

$$\Delta_2 = i \langle X | H_z | Y \rangle, \quad (19)$$

$$\Delta_3 = i \langle Y | H_x | Z \rangle = i \langle Z | H_y | X \rangle, \quad (20)$$

where H_σ is the orbital part of the SOC operator, Eq. (8).

In the quasi-cubic approximation, one considers $\{|X\rangle, |Y\rangle, |Z\rangle\}$ approximately as partners under the Γ_4 irrep of T_d^2 . This yields $\Delta_2 = \Delta_3$, and $\Delta_1 \approx 0$, but a correction $\Delta_1 \approx \Delta_{\text{cr}}$ is kept to account for the hexagonal crystal field. If we consider that the wurtzite potential can be written as $V_{\text{WZ}} = V_{\text{ZB}} + \Delta V$, where V_{ZB} is the zincblende potential and ΔV is the perturbation that breaks the cubic symmetry, then $\Delta_1 = \langle Z | \Delta V | Z \rangle - \langle X | \Delta V | X \rangle \approx 0$ to first-order in Löwdin perturbation theory, since $|X\rangle$ and $|Z\rangle$ are partners under the cubic group. Consequently, $\Delta_1 \approx \Delta_{\text{cr}}$ arises from second-order contributions, analogous to the emergent quasisymmetry picture from Sec. II A, but achieved through compatibility relations rather than group extension. Moreover, to leading order one obtains $A_1 - A_2 = -A_3 = 2A_4$, $A_3 + 4A_5 = \sqrt{2}A_6$, and $A_7 = 0$ [46]. The quasi-cubic validity is typically verified by $\Delta_3/\Delta_2 \approx 1$. From DFT-fitted parameters [Fig. 6(a)], we find that $\Delta_3/\Delta_2 \sim 1$ for GaP and CdS, while it deviates from the perfect ratio by 20% – 50% for GaN and ZnO [129–133]. Particu-

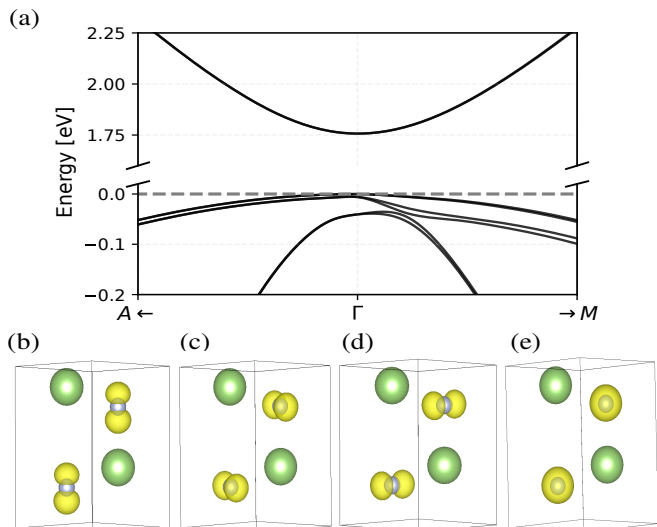


Figure 6. (a) Band structure of wurtzite GaN obtained from Quantum ESPRESSO along the high-symmetry path A- Γ -M. The energy axis is broken to suppress an intermediate energy range and improve the visualization of the valence and conduction bands. A zoom in the k -axis around the Γ point along A- Γ -M highlights the bands in the vicinity of Γ . (b)-(e) Charge density distributions (yellow isosurfaces) at Γ corresponding to the three uppermost valence bands and the first conduction band. Green and gray spheres denote Ga and N atoms.

larly, for GaP the first and second conduction bands are inverted [134, 135], such that the first conduction band has $X(X^2 - 3Y^2)$ character, which does not have a well-defined partner under the cubic group, and thus its compatibility with the C_{6v}^4 irreps is ill-defined (see Table I), breaking the quasi-cubic approximation.

In contrast, inversion \mathcal{I} acts as an alternative quasisymmetry within the subspace of top valence bands and lowest conduction bands, yielding quasisymmetry group $D_{6h}^4 = C_{6v}^4 \otimes \{E, \mathcal{I}\}$. Wavefunctions in this subspace are strongly localized on anion sites [Fig. 6(b)-(e)]. The representation matrices $Q_{mn} = \langle m | \mathcal{I} | n \rangle$ [Figs. 5(e-h)] yield $\epsilon \sim 0.9$ for GaN, GaP and CdS, while for ZnO we get $\epsilon \sim 0.76$, confirming approximate inversion symmetry. Diagonal entries of Q_{mn} show valence bands are odd under inversion (p-like), while conduction bands are even (s-like) for GaN, CdS and ZnO, and odd for GaP [134, 135]. The constraints induced by \mathcal{I} on the Hamiltonian from Eq. (16) are less restrictive than those of the quasi-cubic approximation; they lead only to $A_7 = 0$, $\alpha_i = 0$ (kSOC terms), which is reasonable for all wurtzites.

The inversion quasisymmetry constraints can be further applied to optical selection rules involving the first conduction band of GaP, which is odd under quasi-inversion in the QS group D_{6h}^4 . The optical transition oscillator strengths depend on electric dipole matrix elements $\mathbf{d} = -e\mathbf{r}$. Within the crystal double group C_{6v}^4 , the Γ_9 valence to Γ_8 conduction band transition in GaP is allowed for light perpendicular to the c axis,

Table II. Irreducible representations for the α , β , and γ states, and the angular momentum R_ν (orbital part of the SOC operators) for $\nu = \{x, y, z\}$ under the symmetry groups discussed in Section III B.

	α	β	γ	R_x	R_y	R_z
C_{2v}^T	A_1	B_2	B_1	A_2	B_1	B_2
C_{2v}^W	A_1	B_2	A_1	B_2	B_1	A_2
D_{2h}^R	A_g	B_{2u}	B_{1u}	B_{3g}	B_{2g}	B_{1g}

since $\Gamma_9 \otimes \Gamma_8 = \Gamma_5(x, y) \oplus \Gamma_6$. Under quasisymmetry group D_{6h}^4 , the transition becomes first-order forbidden because both bands belong to odd quasi-irreps; thus $\Gamma_9^- \otimes \Gamma_8^- = \Gamma_5^+ \oplus \Gamma_6^+$ contains no vector irrep. Moreover, the suppression of this matrix element due to QS can be quantified via the metric ϵ . We can split the wavefunctions into $|\Gamma_\nu\rangle = \sqrt{\epsilon}|\Gamma_\nu^-\rangle + \sqrt{1-\epsilon}|\Gamma_\nu^+\rangle$, where $|\Gamma_\nu^\mp\rangle$ carry the odd (quasisymmetric) and even (small correction) components. Thus, the dipole matrix element can be written as

$$\langle \Gamma_9 | \mathbf{d} | \Gamma_8 \rangle = \epsilon \langle \Gamma_9^- | \mathbf{d} | \Gamma_8^- \rangle + (1-\epsilon) \langle \Gamma_9^+ | \mathbf{d} | \Gamma_8^+ \rangle + \sqrt{\epsilon(1-\epsilon)} [\langle \Gamma_9^- | \mathbf{d} | \Gamma_8^+ \rangle + \langle \Gamma_9^+ | \mathbf{d} | \Gamma_8^- \rangle]. \quad (21)$$

The first and second terms vanish by symmetry constraints, while the others terms are suppressed, since the spectral weight of the $|\Gamma_\nu^+\rangle$ component is diminished outside the QS subspace, as shown in Fig. 5. For GaP, with $\epsilon \sim 0.9$, the factor $\sqrt{\epsilon(1-\epsilon)} \sim 0.3$ indicates a $\sim 70\%$ suppression of the transition intensity compared to a fully allowed transition, consistent with experimental observations of weak A-transitions in GaP [134].

B. Quasisymmetries II: inheritance picture

We revisit AgLa [93] to clarify its quasisymmetry. AgLa [Fig. 7(a)] is a tetragonal compound in space group $P4/mmm$ (D_{4h}^1). The Brillouin zone is shown in Fig. 7(b). Without SOC, the band structure exhibits crossings along paths A-R (denoted T) and R-X (denoted W) involving three states $|\alpha\rangle$, $|\beta\rangle$, and $|\gamma\rangle$, dominated respectively by orbitals $\alpha = \text{Ag}(d_{yz}) + \text{La}(d_{x^2-y^2})$, $\beta = \text{Ag}(p_z) + \text{La}(f_{y(3x^2-y^2)})$, and $\gamma = \text{Ag}(p_y) + \text{La}(f_{z(x^2-y^2)})$. Including SOC, Fig. 7(c-d) shows anticrossing gaps are small along the T-path (~ 7 meV for $\alpha-\beta$, ~ 20 meV for $\alpha-\gamma$ anticrossings), while along the W-path the $\beta-\gamma$ anticrossing gap is larger (~ 80 meV).

Both T and W paths are invariant under C_{2v} , but with different axes: $C_{2v}^T = \{E, C_2(x), M_z, M_y\}$ and $C_{2v}^W = \{E, C_2(z), M_y, M_x\}$. Table II shows irreps of α , β , γ under these groups and D_{2h} at R. Selection rules along T give $A_1 \otimes B_2 = B_2$ and $A_1 \otimes B_1 = B_1$ for $\alpha-\beta$ and $\alpha-\gamma$ crossings, indicating finite SOC from σ_z and σ_y couplings. Along W, the $\beta-\gamma$ crossing requires σ_x since $B_2 \otimes A_1 = B_2$. Therefore, under crystal groups C_{2v}^T and C_{2v}^W , all crossings in Fig. 7(c) should open SOC gaps.

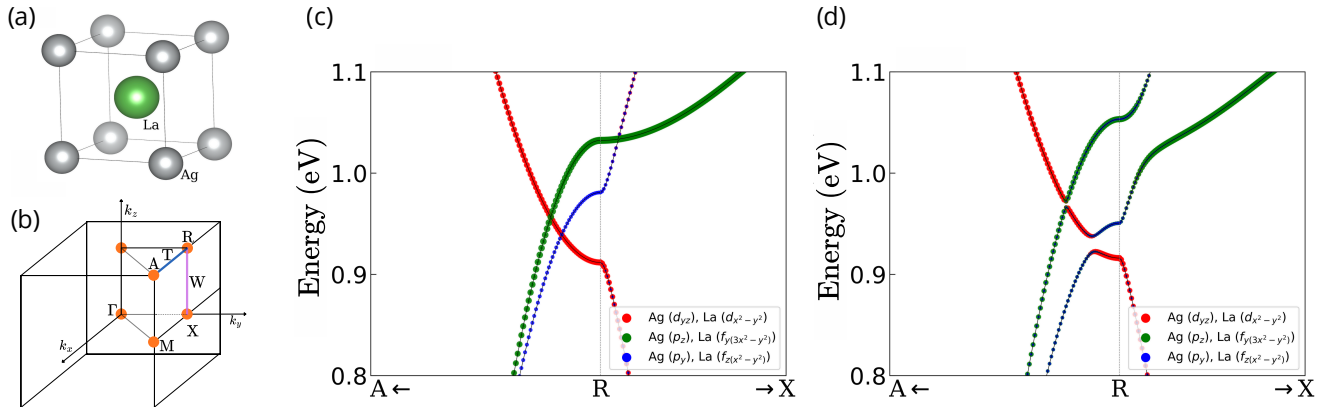


Figure 7. (a) Simple cubic unit cell of AgLa, with La (green) and Ag (gray) atoms. (b) Brillouin zone of the AgLa crystal, highlighting the high-symmetry paths $T = R-A$ and $W = R-X$. (c,d) AgLa band structure along the $A-R-X$ path without and with spin-orbit coupling, respectively. The color coding denotes the dominant orbital-projected contributions indicated in the legend. SOC lifts the band degeneracies at the crossing points, inducing band splittings. The splittings are noticeably smaller along the T path, in contrast with the larger splitting along the W path.

Reference [93] shows quasisymmetries can emerge when C_{2v} is extended by S_4 , C_4 , or inversion \mathcal{I} symmetries. For crossings in Fig. 7(c), these extensions do not leave T or W paths invariant, ruling out the emergent symmetry picture from Sec. II A and Ref. [93] itself. Instead, spatial inversion \mathcal{I} acts as a QS under the inheritance picture (Sec. II B), yielding $D_{2h} = C_{2v} \otimes \{E, \mathcal{I}\}$ as the quasisymmetry group from proximity to the R point, without requiring T or W path invariance.

To illustrate the QS constraints, we analyze SOC matrix elements for each crossing. From Eq. (11) and selection rules from Table II, the symmetry-allowed contributions are

$$\langle \alpha | H_z | \beta \rangle_T = -\frac{1}{4} \alpha^2 \langle \alpha | V_y | \beta \rangle_R \delta k_x, \quad (22)$$

$$\langle \alpha | H_y | \gamma \rangle_T = +\frac{1}{4} \alpha^2 \langle \alpha | V_z | \gamma \rangle_R \delta k_x, \quad (23)$$

$$\langle \beta | H_x | \gamma \rangle_W = +\frac{1}{4} \alpha^2 \langle \beta | (V_y p_z - V_z p_y) | \gamma \rangle_R, \quad (24)$$

where H_σ is defined in Eq. (8), $V_\nu = \partial V / \partial x_\nu$. The indices on the bra-kets indicate that the matrix elements are evaluated at the crossings along the T or W paths, or at the R point. For the crossings along T , only δk -terms are allowed, while along W , only p-terms contribute. Since δk -SOC terms are typically small in $\mathbf{k} \cdot \mathbf{p}$ models, k-term contributions are smaller than p-terms, explaining the smaller gaps along T versus W .

IV. CONCLUSIONS

We established a comprehensive framework for characterizing quasisymmetry (QS) in crystalline materials combining group-theoretical analysis, $\mathbf{k} \cdot \mathbf{p}$ modeling, and

first-principles simulations. We consider quasisymmetries emerging through two distinct pictures: (i) wavefunction localization on sublattices invariant under the quasisymmetry, or (ii) quasisymmetry inheritance from nearby high-symmetry points. Our approach extends the original quasisymmetry proposal [91, 92] and the point group classification from Ref. [93] by identifying emergence mechanisms and distinguishing between sublattice localization and inheritance pictures. This introduces *predictive power* to quasisymmetries, which can be used to understand and engineer spin splittings in semiconductors, modulate optical transition strengths, and design topological phase transitions controlled by perturbations.

The calculated representation matrices $Q_{m,n}$ allow us to quantify quasisymmetry via the metric ϵ . Combined with the group-subgroup diagram from Ref. [93] (Fig. 2), this enables future high-throughput identification and classification of materials by quasisymmetry degree. We propose a numerical procedure to quantitatively verify first-order SOC gap intensity, confirming significant suppression of first-order contributions.

We applied our methodology to various materials. For Sn/SiC, we unified apparently contradictory interpretations: Ref. [94] invokes emergent M_y quasisymmetry within the RL subspace, while Ref. [95] describes an $SU(2)$ quasisymmetry. We show that the M_y quasisymmetry, and its C_3 conjugated partners, yield a sufficient subset of $SU(2)$ operators within the RL subspace. For AgLa, Ref. [93] introduces inversion as quasisymmetry despite non-invariant Bloch phases along T and W paths. Our inheritance picture solves this issue by transferring matrix elements to the inversion-invariant high-symmetry point R . For wurtzites, we argue that the quasi-cubic approximation can be seen as a quasisymmetry generated through compatibility relations between crystal groups linked by the common subgroup C_3^1 . Addi-

tionally, wurtzites allow for a second inversion quasisymmetry, which explains the weak A-transition oscillator strength in GaP.

As a final remark, we notice that the quasisymmetry in CoSi [91, 92] may relate to our inheritance picture. However, its nonsymmorphic lattice (space group $P2_13$) requires careful evaluation beyond the present scope.

ACKNOWLEDGMENTS

We acknowledge useful conversations with Jinwoong Kim and David Vanderbilt about approaches to calcu-

late the spin-orbit couplings using `wannier90`, and useful conversations with Paulo E. Faria Junior about the DFT limitations to extract the spin-orbit coupling via the $\mathbf{k} \cdot \mathbf{p}$ method. This work was supported by the funding agencies CNPq, CAPES, and FAPEMIG. Particularly, E.V.C.L. and T.M.S. acknowledge CENAPAD-SP (project proj483) and LNCC (project SCAFMat2) for the computational time, and G.J.F. acknowledges funding from the FAPEMIG grant PPM-00798-18.

-
- [1] G. F. Koster, J. O. Dimmock, R. G. Wheeler, and H. Statz, *The Properties of the Thirty-Two Point Groups* (M.I.T. Press, Cambridge, Mass., 1963).
 - [2] G. Bir and G. Pikus, *Symmetry and Strain-induced Effects in Semiconductors*, A Halsted Press book (Wiley, 1974).
 - [3] R. Winkler, *Spin-orbit coupling effects in two-dimensional electron and hole systems*, Springer tracts in modern physics (Springer, Berlin, 2003).
 - [4] M. Dresselhaus, G. Dresselhaus, and A. Jorio, *Group Theory: Application to the Physics of Condensed Matter*, SpringerLink: Springer e-Books (Springer Berlin Heidelberg, 2007).
 - [5] M. Willatzen and L. C. L. Y. Voon, *The kp method: electronic properties of semiconductors*, Vol. 1 (Springer, 2009).
 - [6] Y. Peter and M. Cardona, *Fundamentals of Semiconductors: Physics and Materials Properties* (Springer Science & Business Media, 2010).
 - [7] A. Altland and M. R. Zirnbauer, Nonstandard symmetry classes in mesoscopic normal-superconducting hybrid structures, *Phys. Rev. B* **55**, 1142 (1997).
 - [8] C.-K. Chiu, J. C. Y. Teo, A. P. Schnyder, and S. Ryu, Classification of topological quantum matter with symmetries, *Rev. Mod. Phys.* **88**, 035005 (2016).
 - [9] B. Bradlyn, L. Elcoro, J. Cano, M. G. Vergniory, Z. Wang, C. Felser, M. I. Aroyo, and B. A. Bernevig, Topological quantum chemistry, *Nature* **547**, 298 (2017).
 - [10] J. Cano, B. Bradlyn, Z. Wang, L. Elcoro, M. G. Vergniory, C. Felser, M. I. Aroyo, and B. A. Bernevig, Building blocks of topological quantum chemistry: Elementary band representations, *Phys. Rev. B* **97**, 035139 (2018).
 - [11] J. Cano and B. Bradlyn, Band representations and topological quantum chemistry, *Annu. Rev. Condens. Ma. P.* **12**, 225–246 (2021).
 - [12] C. L. Kane and E. J. Mele, Quantum spin hall effect in graphene, *Phys. Rev. Lett.* **95**, 226801 (2005).
 - [13] C. L. Kane and E. J. Mele, Z_2 topological order and the quantum spin hall effect, *Phys. Rev. Lett.* **95**, 146802 (2005).
 - [14] B. A. Bernevig, T. L. Hughes, and S.-C. Zhang, Quantum spin hall effect and topological phase transition in hgte quantum wells, *Science* **314**, 1757 (2006).
 - [15] M. König, S. Wiedmann, C. Brüne, A. Roth, H. Buhmann, L. W. Molenkamp, X.-L. Qi, and S.-C. Zhang, Quantum spin hall insulator state in hgte quantum wells, *Science* **318**, 766 (2007).
 - [16] D. Hsieh, D. Qian, L. Wray, Y. Xia, Y. S. Hor, R. J. Cava, and M. Z. Hasan, A topological dirac insulator in a quantum spin hall phase, *Nature* **452**, 970 (2008).
 - [17] D. Hsieh, Y. Xia, D. Qian, L. Wray, J. H. Dil, F. Meier, J. Osterwalder, L. Patthey, J. G. Checkelsky, N. P. Ong, A. V. Fedorov, H. Lin, A. Bansil, D. Grauer, Y. S. Hor, R. J. Cava, and M. Z. Hasan, A tunable topological insulator in the spin helical dirac transport regime, *Nature* **460**, 1101 (2009).
 - [18] M. Z. Hasan and C. L. Kane, Colloquium: Topological insulators, *Rev. Mod. Phys.* **82**, 3045 (2010).
 - [19] L. Fu, Topological crystalline insulators, *Phys. Rev. Lett.* **106**, 10.1103/physrevlett.106.106802 (2011).
 - [20] Y. Tanaka, Z. Ren, T. Sato, K. Nakayama, S. Souma, T. Takahashi, K. Segawa, and Y. Ando, Experimental realization of a topological crystalline insulator in snTe, *Nat. Phys.* **8**, 800–803 (2012).
 - [21] P. Dziawa, B. J. Kowalski, K. Dybko, R. Buczko, A. Szczerbakow, M. Szot, E. Łusakowska, T. Balasubramanian, B. M. Wojek, M. H. Berntsen, O. Tjernberg, and T. Story, Topological crystalline insulator states in pb1-xsnxse, *Nat. Mater.* **11**, 1023 (2012).
 - [22] X. Wan, A. M. Turner, A. Vishwanath, and S. Y. Savrasov, Topological semimetal and fermi-arc surface states in the electronic structure of pyrochlore iridates, *Phys. Rev. B* **83**, 205101 (2011).
 - [23] A. A. Burkov and L. Balents, Weyl semimetal in a topological insulator multilayer, *Phys. Rev. Lett.* **107**, 127205 (2011).
 - [24] B. Singh, A. Sharma, H. Lin, M. Z. Hasan, R. Prasad, and A. Bansil, Topological electronic structure and weyl semimetal in the tlbise2 class of semiconductors, *Phys. Rev. B* **86**, 115208 (2012).
 - [25] S. M. Young, S. Zaheer, J. C. Y. Teo, C. L. Kane, E. J. Mele, and A. M. Rappe, Dirac semimetal in three dimensions, *Phys. Rev. Lett.* **108**, 140405 (2012).
 - [26] N. P. Armitage, E. J. Mele, and A. Vishwanath, Weyl and dirac semimetals in three-dimensional solids, *Rev. Mod. Phys.* **90**, 015001 (2018).
 - [27] M. Z. Hasan, S.-Y. Xu, I. Belopolski, and S.-M. Huang, Discovery of weyl fermion semimetals and topological

- fermi arc states, *Annu. Rev. Condens. Ma. P.* **8**, 289–309 (2017).
- [28] A. P. Schnyder, S. Ryu, A. Furusaki, and A. W. W. Ludwig, Classification of topological insulators and superconductors in three spatial dimensions, *Phys. Rev. B* **78**, 195125 (2008).
- [29] A. Kitaev, V. Lebedev, and M. Feigel'man, Periodic table for topological insulators and superconductors, in *AIP Conference Proceedings* (AIP, 2009) p. 22–30.
- [30] M. Sato and Y. Ando, Topological superconductors: a review, *Rep. Prog. Phys.* **80**, 076501 (2017).
- [31] T. Neupert, M. M. Denner, J.-X. Yin, R. Thomale, and M. Z. Hasan, Charge order and superconductivity in kagome materials, *Nat. Phys.* **18**, 137–143 (2021).
- [32] Z. Zhang, Z. Wu, C. Fang, F.-c. Zhang, J. Hu, Y. Wang, and S. Qin, Topological superconductivity from unconventional band degeneracy with conventional pairing, *Nat. Commun.* **15**, 10.1038/s41467-024-52156-1 (2024).
- [33] L. Šmejkal, J. Sinova, and T. Jungwirth, Beyond conventional ferromagnetism and antiferromagnetism: A phase with nonrelativistic spin and crystal rotation symmetry, *Phys. Rev. X* **12**, 031042 (2022).
- [34] L. Šmejkal, J. Sinova, and T. Jungwirth, Emerging research landscape of altermagnetism, *Phys. Rev. X* **12**, 040501 (2022).
- [35] J. Krempaský, L. Šmejkal, S. W. D'Souza, M. Hajaoui, G. Springholz, K. Uhlířová, F. Alarab, P. C. Constantinou, V. Strocov, D. Usanov, W. R. Pudelko, R. González-Hernández, A. Birk Hellenes, Z. Jansa, H. Reichlová, Z. Šobáň, R. D. Gonzalez Betancourt, P. Wadley, J. Sinova, D. Kriegner, J. Minár, J. H. Dil, and T. Jungwirth, Altermagnetic lifting of kramers spin degeneracy, *Nature* **626**, 517–522 (2024).
- [36] T. Osumi, S. Souma, T. Aoyama, K. Yamauchi, A. Honma, K. Nakayama, T. Takahashi, K. Ohgushi, and T. Sato, Observation of a giant band splitting in altermagnetic mnte, *Phys. Rev. B* **109**, 115102 (2024).
- [37] J. C. Slater and G. F. Koster, Simplified lcao method for the periodic potential problem, *Phys. Rev.* **94**, 1498–1524 (1954).
- [38] C. M. Goringe, D. R. Bowler, and E. Hernández, Tight-binding modelling of materials, *Rep. Prog. Phys.* **60**, 1447 (1997).
- [39] J. M. Luttinger and W. Kohn, Motion of electrons and holes in perturbed periodic fields, *Phys. Rev.* **97**, 869 (1955).
- [40] E. O. Kane, Energy band structure in p-type germanium and silicon, *J. Phys. Chem. Solids* **1**, 82 (1956).
- [41] E. O. Kane, Band structure of indium antimonide, *J. Phys. Chem. Solids* **1**, 249 (1957).
- [42] J. M. Luttinger and W. Kohn, Motion of Electrons and Holes in Perturbed Periodic Fields, *Phys. Rev.* **97**, 869 (1955).
- [43] M. Cardona and F. H. Pollak, Energy-Band Structure of Germanium and Silicon: The kp Method, *Phys. Rev.* **142**, 530 (1966).
- [44] J. Hopfeld, Fine structure in the optical absorption edge of anisotropic crystals, *J. Phys. Chem. Solids* **15**, 97 (1960).
- [45] L. C. Lew Yan Voon, M. Willatzen, M. Cardona, and N. E. Christensen, Terms linear in k in the band structure of wurtzite-type semiconductors, *Phys. Rev. B* **53**, 10703 (1996).
- [46] S. L. Chuang and C. S. Chang, kp method for strained wurtzite semiconductors, *Phys. Rev. B* **54**, 2491 (1996).
- [47] E. Gutsche and E. Jahne, Spin-Orbit Splitting of the Valence Band of Wurtzite Type Crystals, *Phys. Status Solidi B* **19**, 823 (1967).
- [48] G. Pikus, A new method of calculating the energy spectrum of carriers in semiconductors. i. neglecting spin-orbit interaction, *Sov. Phys. J. Exp. Theor. Phys.* **14**, 898 (1962).
- [49] Y. A. Bychkov and É. I. Rashba, Properties of a 2d electron gas with lifted spectral degeneracy, *JETP lett* **39**, 78 (1984).
- [50] G. Dresselhaus, Spin-orbit coupling effects in zinc blende structures, *Phys. Rev.* **100**, 580 (1955).
- [51] C. Mera Acosta, L. Yuan, G. M. Dalpian, and A. Zunger, Different shapes of spin textures as a journey through the brillouin zone, *Phys. Rev. B* **104**, 104408 (2021).
- [52] W. Liu and Y. Xu, *Spintronic 2D materials: fundamentals and applications* (Elsevier, 2019).
- [53] A. Splendiani, L. Sun, Y. Zhang, T. Li, J. Kim, C.-Y. Chim, G. Galli, and F. Wang, Emerging photoluminescence in monolayer mos2, *Nano Lett.* **10**, 1271 (2010).
- [54] D. Xiao, G.-B. Liu, W. Feng, X. Xu, and W. Yao, Coupled spin and valley physics in monolayers of mos₂ and other group-vi dichalcogenides, *Phys. Rev. Lett.* **108**, 196802 (2012).
- [55] A. K. Geim and I. V. Grigorieva, Van der waals heterostructures, *Nature* **499**, 419–425 (2013).
- [56] K. F. Mak, C. Lee, J. Hone, J. Shan, and T. F. Heinz, Atomically thin mos2: a new direct-gap semiconductor, *Physical review letters* **105**, 136805 (2010).
- [57] K. M. McCreary, A. T. Hanbicki, G. G. Jernigan, J. C. Culbertson, and B. T. Jonker, Synthesis of large-area ws2 monolayers with exceptional photoluminescence, *Scientific reports* **6**, 19159 (2016).
- [58] T. Woźniak, P. E. Faria Junior, G. Seifert, A. Chaves, and J. Kunstmann, Exciton *g* factors of van der waals heterostructures from first-principles calculations, *Phys. Rev. B* **101**, 10.1103/physrevb.101.235408 (2020).
- [59] V. Singh, D. J. Late, and S. Rath, Tunable light emission from chemical vapor deposited two-dimensional mose2 by layer variation and s incorporation, *Journal of Vacuum Science & Technology A* **38** (2020).
- [60] A. M. Jones, H. Yu, N. J. Ghimire, S. Wu, G. Aivazian, J. S. Ross, B. Zhao, J. Yan, D. G. Mandrus, D. Xiao, *et al.*, Optical generation of excitonic valley coherence in monolayer wse2, *Nature nanotechnology* **8**, 634 (2013).
- [61] P. E. Faria Junior, D. Hernangómez-Pérez, T. Amit, J. Fabian, and S. Refaely-Abramson, Generalized many-body exciton *g* factors: Magnetic hybridization and nonmonotonic rydberg series in monolayer wse2, *Phys. Rev. B* **112**, L241404 (2025).
- [62] Q. H. Wang, K. Kalantar-Zadeh, A. Kis, J. N. Coleman, and M. S. Strano, Electronics and optoelectronics of two-dimensional transition metal dichalcogenides, *Nature Nanotechnology* **7**, 699–712 (2012).
- [63] M. Chhowalla, H. S. Shin, G. Eda, L.-J. Li, K. P. Loh, and H. Zhang, The chemistry of two-dimensional layered transition metal dichalcogenide nanosheets, *Nature Chemistry* **5**, 263–275 (2013).
- [64] K. F. Mak and J. Shan, Photonics and optoelectronics of 2d semiconductor transition metal dichalcogenides, *Nature Photonics* **10**, 216–226 (2016).

- [65] S. Manzeli, D. Ovchinnikov, D. Pasquier, O. V. Yazyev, and A. Kis, 2d transition metal dichalcogenides, *Nature Reviews Materials* **2**, [10.1038/natrevmats.2017.33](https://doi.org/10.1038/natrevmats.2017.33) (2017).
- [66] M. Glazov, A. Arora, A. Chaves, and Y. G. Gobato, Excitons in two-dimensional materials and heterostructures: Optical and magneto-optical properties, *MRS Bull.* **49**, 899–913 (2024).
- [67] S. Deb, J. Krause, P. E. Faria Junior, M. A. Kempf, R. Schwartz, K. Watanabe, T. Taniguchi, J. Fabian, and T. Korn, Excitonic signatures of ferroelectric order in parallel-stacked mos2, *Nat. Commun.* **15**, [10.1038/s41467-024-52011-3](https://doi.org/10.1038/s41467-024-52011-3) (2024).
- [68] G. H. Han, D. L. Duong, D. H. Keum, S. J. Yun, and Y. H. Lee, van der waals metallic transition metal dichalcogenides, *Chemical Reviews* **118**, 6297–6336 (2018).
- [69] M. Yagmurcukardes, Y. Qin, S. Ozen, M. Sayyad, F. M. Peeters, S. Tongay, and H. Sahin, Quantum properties and applications of 2d janus crystals and their superlattices, *Applied Physics Reviews* **7**, [10.1063/1.5135306](https://doi.org/10.1063/1.5135306) (2020).
- [70] X. Zheng, Y. Zhou, and Y. Guo, Symmetry manipulation of two-dimensional semiconductors by janus structure, *Accounts of Materials Research* **6**, 124–128 (2024).
- [71] L. Zhang, Z. Yang, T. Gong, R. Pan, H. Wang, Z. Guo, H. Zhang, and X. Fu, Recent advances in emerging janus two-dimensional materials: from fundamental physics to device applications, *Journal of Materials Chemistry A* **8**, 8813–8830 (2020).
- [72] W.-J. Yin, H.-J. Tan, P.-J. Ding, B. Wen, X.-B. Li, G. Teobaldi, and L.-M. Liu, Recent advances in low-dimensional janus materials: theoretical and simulation perspectives, *Materials Advances* **2**, 7543–7558 (2021).
- [73] G. Garcia-Arellano, K. Boujdaria, M. Chamarro, and C. Testelin, Landé g factors in tetragonal halide perovskite: A multiband k.p model, *Phys. Rev. B* **106**, 165201 (2022).
- [74] S. D. Stranks and H. J. Snaith, Metal-halide perovskites for photovoltaic and light-emitting devices, *Nature Nanotechnology* **10**, 391 (2015).
- [75] A. K. Jena, A. Kulkarni, and T. Miyasaka, Halide perovskite photovoltaics: Background, status, and future prospects, *Chemical Reviews* **119**, 3036 (2019).
- [76] M. Naguib, V. N. Mochalin, M. W. Barsoum, and Y. Gogotsi, 25th anniversary article: Mxenes: A new family of two-dimensional materials, *Advanced Materials* **26**, 992–1005 (2013).
- [77] M. Khazaei, A. Ranjbar, M. Arai, T. Sasaki, and S. Yunoki, Electronic properties and applications of mxenes: a theoretical review, *Journal of Materials Chemistry C* **5**, 2488–2503 (2017).
- [78] S. Guha, A. Kabiraj, and S. Mahapatra, High-throughput design of functional-engineered mxene transistors with low-resistive contacts, *npj Computational Materials* **8**, [10.1038/s41524-022-00885-6](https://doi.org/10.1038/s41524-022-00885-6) (2022).
- [79] J. Li, R.-L. Chu, J. K. Jain, and S.-Q. Shen, Topological Anderson insulator, *Phys. Rev. Lett.* **102**, 136806 (2009).
- [80] C. W. Groth, M. Wimmer, A. R. Akhmerov, J. Tworzydło, and C. W. J. Beenakker, Theory of the topological Anderson insulator, *Phys. Rev. Lett.* **103**, 196805 (2009).
- [81] S. Stützer, Y. Plotnik, Y. Lumer, P. Titum, N. H. Lindner, M. Segev, M. C. Rechtsman, and A. Szameit, Photonic topological anderson insulators, *Nature* **560**, 461–465 (2018).
- [82] J. Zhang, Z.-Q. Zhang, S.-g. Cheng, and H. Jiang, Topological anderson insulator via disorder-recovered average symmetry, *Phys. Rev. B* **106**, [10.1103/physrevb.106.195304](https://doi.org/10.1103/physrevb.106.195304) (2022).
- [83] M. D. Caio, G. Möller, N. R. Cooper, and M. J. Bhaseen, Topological marker currents in chern insulators, *Nat. Phys.* **15**, 257–261 (2019).
- [84] D. Varjas, M. Fruchart, A. R. Akhmerov, and P. M. Perez-Piskunow, Computation of topological phase diagram of disordered $\text{pb}_{1-x}\text{sn}_x\text{Te}$ using the kernel polynomial method, *Phys. Rev. Res.* **2**, [10.1103/physrevresearch.2.013229](https://doi.org/10.1103/physrevresearch.2.013229) (2020).
- [85] B. D. Assunção, G. J. Ferreira, and C. H. Lewenkopf, Phase transitions and scale invariance in topological anderson insulators, *Phys. Rev. B* **109**, L201102 (2024).
- [86] E. Kroumova, M. I. Aroyo, J. M. Perez-Mato, S. Ivantchev, J. M. Igartua, and H. Wondratschek, Pseudo: a program for a pseudosymmetry search, *J. Appl. Crystallogr.* **34**, 783 (2001).
- [87] P. H. Zwart, R. W. Grosse-Kunstleve, A. A. Lebedev, G. N. Murshudov, and P. D. Adams, Surprises and pitfalls arising from (pseudo)symmetry, *Acta Crystallogr. D* **64**, 99–107 (2007).
- [88] C. Capillas, E. S. Tasci, G. de la Flor, D. Orobengoa, J. M. Perez-Mato, and M. I. Aroyo, A new computer tool at the bilbao crystallographic server to detect and characterize pseudosymmetry, *Z. Kristallogr. Cryst. Mater.* **226**, 186 (2011).
- [89] G. Nolze, T. Tokarski, and L. Rychlowski, Use of electron backscatter diffraction patterns to determine the crystal lattice. part 3. pseudosymmetry, *J. Appl. Crystallogr.* **56**, 367–380 (2023).
- [90] F. Crasto de Lima and G. J. Ferreira, High-degeneracy points protected by site-permutation symmetries, *Phys. Rev. B* **101**, 041107 (2020).
- [91] C. Guo, L. Hu, C. Putzke, J. Diaz, X. Huang, K. Manna, F.-R. Fan, C. Shekhar, Y. Sun, C. Felser, C. Liu, B. A. Bernevig, and P. J. W. Moll, Quasi-symmetry-protected topology in a semi-metal, *Nat. Phys.* **18**, 813 (2022).
- [92] L.-H. Hu, C. Guo, Y. Sun, C. Felser, L. Elcoro, P. J. W. Moll, C.-X. Liu, and B. A. Bernevig, Hierarchy of quasisymmetries and degeneracies in the CoSi family of chiral crystal materials, *Phys. Rev. B* **107**, 125145 (2023).
- [93] J. Li, A. Zhang, Y. Liu, and Q. Liu, Group Theory on Quasisymmetry and Protected Near Degeneracy, *Phys. Rev. Lett.* **133**, 026402 (2024).
- [94] K. Yaji, A. Visikovskiy, T. Iimori, K. Kuroda, S. Hayashi, T. Kajiwara, S. Tanaka, F. Komori, and S. Shin, Coexistence of Two Types of Spin Splitting Originating from Different Symmetries, *Phys. Rev. Lett.* **122**, 126403 (2019).
- [95] L. L. Tao, J. Li, Y. Liu, X. Wang, Y. Sui, B. Song, M. Y. Zhuravlev, and Q. Liu, Rashba-like spin splitting around non-time-reversal-invariant momenta, *Phys. Rev. B* **107**, 235138 (2023).
- [96] L. L. Tao, Spin polarization in materials described by noncentrosymmetric and nonsymmorphic space groups, *Phys. Rev. B* **110**, L121125 (2024).
- [97] L. Liu, Y. Liu, J. Li, H. Wu, and Q. Liu, Quantum spin hall effect protected by spin $u(1)$ quasisymmetry, *Phys. Rev. B* **110**, L161104 (2024).

- [98] L. Liu, Y. Liu, J. Li, H. Wu, and Q. Liu, Orbital doublet driven even-spin chern insulators, *Phys. Rev. B* **110**, 035161 (2024).
- [99] J. Li, F.-R. Fan, and W. Yao, Quasisymmetry enriched gapless criticality at chern insulator transitions (2026), [arXiv:2601.15011 \[cond-mat.mtrl-sci\]](https://arxiv.org/abs/2601.15011).
- [100] A. Zhang, X. Chen, J. Li, P. Liu, Y. Liu, and Q. Liu, Topological charge quadrupole protected by spin-orbit u(1) quasi-symmetry in antiferromagnet ndbipt, *Newton* **1** (2025).
- [101] M. Roig, Y. Yu, R. C. Ekman, A. Kreisel, B. M. Andersen, and D. F. Agterberg, Quasisymmetry-constrained spin ferromagnetism in altermagnets, *Phys. Rev. Lett.* **135**, 016703 (2025).
- [102] M. Kang, M. Lee, and S. Cheon, Subsymmetry protected topology in topological insulators and superconductors, *Phys. Rev. Res.* **6**, 033323 (2024).
- [103] L. L. Tao, Q. Zhang, H. Li, X. Wang, Y. Wang, Y. Sui, B. Song, and M. Y. Zhuravlev, Quasisymmetry protected ising spin-orbit coupling, *Phys. Rev. B* **107**, 10.1103/physrevb.107.155412 (2023).
- [104] J. Ren, C. Liang, and C. Fang, Quasisymmetry groups and many-body scar dynamics, *Phys. Rev. Lett.* **126**, 10.1103/physrevlett.126.120604 (2021).
- [105] J. Ren, Y.-P. Wang, and C. Fang, Quasi-nambu-goldstone modes in many-body scar models, *Phys. Rev. B* **110**, 10.1103/physrevb.110.245101 (2024).
- [106] P.-O. Löwdin, A note on the quantum-mechanical perturbation theory, *J. Chem. Phys.* **19**, 1396 (1951).
- [107] P. Giannozzi, S. Baroni, N. Bonini, M. Calandra, R. Car, C. Cavazzoni, D. Ceresoli, G. L. Chiarotti, M. Cococcioni, I. Dabo, A. D. Corso, S. de Gironcoli, S. Fabris, G. Fratesi, R. Gebauer, U. Gerstmann, C. Gougoussis, A. Kokalj, M. Lazzeri, L. Martin-Samos, N. Marzari, F. Mauri, R. Mazzarello, S. Paolini, A. Pasquarello, L. Paulatto, C. Sbraccia, S. Scandolo, G. Sclauzero, A. P. Seitsonen, A. Smogunov, P. Umari, and R. M. Wentzcovitch, QUANTUM ESPRESSO: a modular and open-source software project for quantum simulations of materials, *J. Phys.: Condens. Matter* **21**, 395502 (2009).
- [108] P. Giannozzi, O. Andreussi, T. Brumme, O. Bunau, M. B. Nardelli, M. Calandra, R. Car, C. Cavazzoni, D. Ceresoli, M. Cococcioni, N. Colonna, I. Carnimeo, A. D. Corso, S. de Gironcoli, P. Delugas, R. A. DiStasio, A. Ferretti, A. Floris, G. Fratesi, G. Fugallo, R. Gebauer, U. Gerstmann, F. Giustino, T. Gorni, J. Jia, M. Kawamura, H.-Y. Ko, A. Kokalj, E. Küçükbenli, M. Lazzeri, M. Marsili, N. Marzari, F. Mauri, N. L. Nguyen, H.-V. Nguyen, A. O. de-la Roza, L. Paulatto, S. Poncé, D. Rocca, R. Sabatini, B. Santra, M. Schlipf, A. P. Seitsonen, A. Smogunov, I. Timrov, T. Thonhauser, P. Umari, N. Vast, X. Wu, and S. Baroni, Advanced capabilities for materials modelling with quantum ESPRESSO, *J. Phys.: Condens. Matter* **29**, 465901 (2017).
- [109] G. Kresse and J. Hafner, Ab initio molecular dynamics for liquid metals, *Phys. Rev. B* **47**, 558 (1993).
- [110] G. Kresse and J. Furthmüller, Efficient iterative schemes for ab initio total-energy calculations using a plane-wave basis set, *Phys. Rev. B* **54**, 11169 (1996).
- [111] A. A. Mostofi, J. R. Yates, G. Pizzi, Y.-S. Lee, I. Souza, D. Vanderbilt, and N. Marzari, An updated version of wannier90: A tool for obtaining maximally-localised wannier functions, *Comput. Phys. Commun.* **185**, 2309 (2014).
- [112] G. Pizzi, V. Vitale, R. Arita, S. Blügel, F. Freimuth, G. Géranton, M. Gibertini, D. Gresch, C. Johnson, T. Koretsune, *et al.*, Wannier90 as a community code: new features and applications, *J. Phys. Condens. Matter* **32**, 165902 (2020).
- [113] A. A. Mostofi, J. R. Yates, Y.-S. Lee, I. Souza, D. Vanderbilt, and N. Marzari, wannier90: A tool for obtaining maximally-localised wannier functions, *Comput. Phys. Commun.* **178**, 685 (2008).
- [114] T. Cole, S. Coh, and D. Vanderbilt, *Python Tight Binding (PythTB)* (2025).
- [115] J. V. V. Cassiano, A. de Leis Araújo, P. E. Faria Junior, and G. J. Ferreira, Dft2kp: Effective kp models from ab-initio data, *SciPost Physics Codebases* **10.21468/scipostphyscodeb.25** (2024).
- [116] M. Iraola, J. L. Mañes, B. Bradlyn, M. K. Horton, T. Neupert, M. G. Vergniory, and S. S. Tsirkin, IrRep: Symmetry eigenvalues and irreducible representations of ab initio band structures, *Comput. Phys. Commun.* **272**, 108226 (2022).
- [117] D. Varjas, T. Ö. Rosdahl, and A. R. Akhmerov, Qsymm: Algorithmic symmetry finding and symmetric hamiltonian generation, *New J. Phys.* **20**, 093026 (2018).
- [118] R. Sakuma, Symmetry-adapted wannier functions in the maximal localization procedure, *Phys. Rev. B* **87**, 235109 (2013).
- [119] S. S. Tsirkin, High performance wannier interpolation of berry curvature and related quantities with wannier-berri code, *NPJ Comput. Mater.* **7**, 10.1038/s41524-021-00498-5 (2021).
- [120] R. Wang, E. A. Lazar, H. Park, A. J. Millis, and C. A. Marianetti, Selectively localized wannier functions, *Phys. Rev. B* **90**, 10.1103/physrevb.90.165125 (2014).
- [121] R. S. Mulliken, Report on notation for the spectra of polyatomic molecules, *J. Chem. Phys.* **23**, 1997–2011 (1955).
- [122] M. Aroyo, J. Perez-Mato, D. Orobengoa, E. Tasci, G. De La Flor, and A. Kirov, Crystallography online: Bilbao crystallographic server, *Bulg. Chem. Commun.* **43**, 183 – 197 (2011), cited by: 637.
- [123] M. I. Aroyo, J. M. Perez-Mato, C. Capillas, E. Kroumova, S. Ivantchev, G. Madariaga, A. Kirov, and H. Wondratschek, Bilbao crystallographic server: I. databases and crystallographic computing programs, *Z. Kristallogr. Cryst. Mater.* **221**, 15–27 (2006).
- [124] M. I. Aroyo, A. Kirov, C. Capillas, J. M. Perez-Mato, and H. Wondratschek, Bilbao crystallographic server. ii. representations of crystallographic point groups and space groups, *Acta Crystallogr. A* **62**, 115–128 (2006).
- [125] K. Kośmider, J. W. González, and J. Fernández-Rossier, Large spin splitting in the conduction band of transition metal dichalcogenide monolayers, *Phys. Rev. B* **88**, 245436 (2013).
- [126] Z. Y. Zhu, Y. C. Cheng, and U. Schwingenschlögl, Giant spin-orbit-induced spin splitting in two-dimensional transition-metal dichalcogenide semiconductors, *Phys. Rev. B* **84**, 10.1103/physrevb.84.153402 (2011).
- [127] P. E. Faria Junior, T. Campos, C. M. Bastos, M. Gmitra, J. Fabian, and G. M. Sipahi, Realistic multiband kp approach from ab initio and spin-orbit coupling ef-

- fects of inas and inp in wurtzite phase, *Phys. Rev. B* **93**, 235204 (2016).
- [128] J. Fu, P. H. Penteado, D. R. Candido, G. J. Ferreira, D. P. Pires, E. Bernardes, and J. C. Egues, Spin-orbit coupling in wurtzite heterostructures, *Phys. Rev. B* **101**, 134416 (2020).
- [129] D. W. Langer, R. N. Euwema, K. Era, and T. Koda, Spin exchange in excitons, the quasicubic model and deformation potentials in ii-vi compounds, *Phys. Rev. B* **2**, 4005–4022 (1970).
- [130] M. Suzuki, T. Uenoyama, and A. Yanase, First-principles calculations of effective-mass parameters of AlN and GaN, *Phys. Rev. B* **52**, 8132 (1995).
- [131] A. A. Yamaguchi, Y. Mochizuki, H. Sunakawa, and A. Usui, Determination of valence band splitting parameters in gan, *J. Appl. Phys.* **83**, 4542–4544 (1998).
- [132] D. J. Dugdale, S. Brand, and R. A. Abram, Direct calculation of $\mathbf{k} \cdot \mathbf{p}$ parameters for wurtzite aln, gan, and inn, *Phys. Rev. B* **61**, 12933 (2000).
- [133] W. R. L. Lambrecht, A. V. Rodina, S. Limpijumngong, B. Segall, and B. K. Meyer, Valence-band ordering and magneto-optic exciton fine structure in zno, *Phys. Rev. B* **65**, 10.1103/physrevb.65.075207 (2002).
- [134] S. Assali, J. Greil, I. Zardo, A. Belabbes, M. W. A. de Moor, S. Koelling, P. M. Koenraad, F. Bechstedt, E. P. A. M. Bakkers, and J. E. M. Haverkort, Optical study of the band structure of wurtzite gap nanowires, *J. Appl. Phys.* **120**, 10.1063/1.4959147 (2016).
- [135] B. C. da Silva, O. D. D. Couto, H. T. Obata, M. M. de Lima, F. D. Bonani, C. E. de Oliveira, G. M. Sipahi, F. Iikawa, and M. A. Cotta, Optical absorption exhibits pseudo-direct band gap of wurtzite gallium phosphide, *Sci. Rep.* **10**, 10.1038/s41598-020-64809-4 (2020).
- [136] J. P. Perdew, K. Burke, and M. Ernzerhof, Generalized gradient approximation made simple, *Phys. Rev. Lett.* **77**, 3865 (1996).
- [137] P. Blaha, K. Schwarz, F. Tran, R. Laskowski, G. K. H. Madsen, and L. D. Marks, Wien2k: An apw+lo program for calculating the properties of solids, *J. Chem. Phys.* **152**, 074101 (2020).

Appendix A: Computational Methodology

First-principles simulations were performed within the framework of density functional theory (DFT), using the Vienna *ab initio* simulation package VASP [109, 110] and Quantum ESPRESSO (QE) [107, 108]. The exchange-correlation energy was treated within the generalized gradient approximation (GGA) using the Perdew-Burke-Ernzerhof (PBE) functional [136]. For the Sn/SiC(0001) - 1×1 system, a kinetic energy cutoff of 500 eV was employed, with the Brillouin zone sampled using an $11 \times 11 \times 1$ Monkhorst-Pack k -mesh. For the AgLa crystal, a cutoff energy of 400 eV and a $9 \times 9 \times 9$ k -mesh were used. In the case of the wurtzite structures GaN and GaP, a higher cutoff of 800 eV was adopted alongside an $8 \times 8 \times 8$ k -mesh to ensure convergence. For the monolayer TMD systems MoS₂ and WSe₂, all band-structure and $\mathbf{k} \cdot \mathbf{p}$ matrix-element calculations were performed using PAW pseudopotentials within QE. For MoS₂, we used

a kinetic-energy cutoff of 100 Ry, an `ecutrho` of 800 Ry and a $10 \times 10 \times 1$ Monkhorst-Pack sampling. For WSe₂, the calculations employed a kinetic-energy cutoff of 100 Ry, an `ecutrho` of 1200 Ry, and the same $10 \times 10 \times 1$ grid. All results for these two systems, except for the charge-density plots, were obtained using PAW pseudopotentials. The charge densities were recalculated using norm-conserving PBE pseudopotentials, since the PAW densities produced nonphysical negative regions in the interstitial space. In all calculations, the atomic positions were fully relaxed until the total energy difference between successive steps was below 10^{-8} eV and the residual forces were smaller than 0.001 eV/Å.

Moreover, throughout this paper we have used several codes to perform the different steps of our analysis. The DFT2kp code [115] and the IrRep code [116] were used to calculate representation matrices and irreducible representations directly from DFT data. The wannier90 [111–113] code was used to construct Wannier functions and tight-binding models, while the PythTB [114] code was used to manipulate the tight-binding models. Finally, the Qsymm code [117] was used to analyze symmetry constraints on the Hamiltonian via the theory of invariants.

All scripts and input files used here are available upon reasonable request.

Appendix B: DFT limitations to extract SOC via $\mathbf{k} \cdot \mathbf{p}$

In principle, one can express the matrix elements of SOC perturbatively via the $\mathbf{k} \cdot \mathbf{p}$ method using the following approach. Consider $|n\rangle$ as spinless eigenstates of the scalar relativistic Hamiltonian H_{SR} , and $|n, \sigma_n\rangle = |n\rangle \otimes |\sigma\rangle$ its extension to include spin $\sigma = \{\uparrow, \downarrow\}$. The first-order matrix element of SOC then reads

$$\langle m, \sigma_m | H^{SOC} | n, \sigma_n \rangle = \frac{\alpha^2}{4} \langle m | \nabla V \times \mathbf{p} | n \rangle \cdot \boldsymbol{\sigma}_{m,n}, \quad (\text{B1})$$

where $\boldsymbol{\sigma}_{m,n} = \langle \sigma_m | \boldsymbol{\sigma} | \sigma_n \rangle$. Now we focus on the orbital term, $\langle m | \nabla V \times \mathbf{p} | n \rangle$ that determines the intensity of this matrix element. We can eliminate V using the commutator $\nabla V = -i[V, \mathbf{p}] \approx -i[H^0, \mathbf{p}]$, often used by Cardona and collaborators [45], with H^0 from Eq. (6). The expression is considered an approximation because it neglects scalar fine structure corrections that would contribute with higher-order ($\propto \alpha^4$) terms to the matrix element of Eq. (B1). Further introducing the completeness relation, the matrix element for the z component reads

$$\langle m | \nabla V \times \mathbf{p} | n \rangle_z = i \sum_{\ell} E_{\ell}^0 \left[p_x^{(m,\ell)} p_y^{(\ell,n)} - (x \leftrightarrow y) \right], \quad (\text{B2})$$

and cyclic permutations of (x, y, z) for the other components. Here $p_{\nu}^{(m,\ell)} = \langle m | p_{\nu} | \ell \rangle$ is the matrix element of momentum that can be directly extracted from DFT data using the DFT2kp code [115] together with band edge

energies E_ℓ^0 . Therefore, in principle we have all elements to compute $\langle m | \nabla V \times \mathbf{p} | n \rangle$ numerically. Unfortunately, this approach fails because the sum over ℓ must run over all states, while typical DFT output for codes like QE [107, 108], VASP [109, 110], and Wien2k [137] does not provide direct access to core states and in practice the sum over ℓ above is effectively truncated. Since core states are the ones that contribute the most to the SOC intensity,

the resulting matrix element with the truncated ℓ -sum lacks the dominant contributions. To overcome this limitation, further work is needed to incorporate momentum matrix elements including core states into DFT2kp, but this is beyond the scope of the current work. In contrast, the wannierization method provides atomistic-like tight-binding models that are appropriate for estimating SOC as discussed in Section IID.